HAL
open science

Orbital scale variations and timescales from the Arctic Ocean

Heiko Pälike, David Spofforth, Matthew O'Regan, J. Gattacceca

To cite this version:

Heiko Pälike, David Spofforth, Matthew O'Regan, J. Gattacceca. Orbital scale variations and timescales from the Arctic Ocean. Paleoceanography, 2008, 23 (1), pp.n/a-n/a. 10.1029/2007PA001490 . hal-03036578

HAL Id: hal-03036578

https://hal.science/hal-03036578

Submitted on 19 Aug 2021

HAL is a multi-disciplinary open access archive for the deposit and dissemination of scientific research documents, whether they are published or not. The documents may come from teaching and research institutions in France or abroad, or from public or private research centers.

L'archive ouverte pluridisciplinaire **HAL**, est destinée au dépôt et à la diffusion de documents scientifiques de niveau recherche, publiés ou non, émanant des établissements d'enseignement et de recherche français ou étrangers, des laboratoires publics ou privés.

Copyright

Orbital scale variations and timescales from the Arctic Ocean

Heiko Pälike,[1] David J. A. Spofforth,[1] Matthew O'Regan,[2] and Jérôme Gattacceca[3]

Received 30 April 2007; revised 23 December 2007; accepted 8 January 2008; published 19 March 2008.

[1] We investigate geochemical measurements from the Arctic Coring Expedition to derive sedimentation rates for selected intervals in the early and middle Eocene. This analysis is performed by quantifying cyclical variations in physical property data and elemental concentrations derived with an X-ray fluorescence (XRF) core scanner. Our results show that physical properties and XRF-derived elemental concentrations are coherent and correlated to each other. Changes in elemental concentrations occur on depth scales from decimeters to meters and correspond to varying contributions of detrital minerals and biogenic silica. We confirm and refine sedimentation rates of the order of 10 to 25 m Ma^{-1}. These rates were obtained independently through biostratigraphic and magnetostratigraphic methods. We observe a strong imprint of astronomically sourced cycles, particularly through climatic precession. This observation allows us to test recently proposed theoretical calculations of insolation.

Citation: Pälike, H., D. J. A. Spofforth, M. O'Regan, and J. Gattacceca (2008), Orbital scale variations and timescales from the Arctic Ocean, *Paleoceanography*, *23*, PA1S10, doi:10.1029/2007PA001490.

1. Introduction

[2] Accurate determinations of ages and sedimentation rates in marine cores are an extremely important prerequisite to decipher past geological, biological and climatological processes. The determination of such rates typically involves multiple approaches, ranging from direct radioisotopic dating [*Kuiper et al.*, 2004] to correlative comparison with existing dated records through magnetostratigraphic or biostratigraphy, or by comparison with theoretically derived astronomical insolation curves [*Laskar et al.*, 1993; *Laskar*, 1999; *Laskar et al.*, 2004], or through a combination of the aforementioned [*Lourens et al.*, 2005].

[3] Advances in data acquisition and techniques have been made recently and enabled the compilation of a highly accurate and resolved geological timescale for the Neogene [*Lourens et al.*, 2005]. These timescales rely fundamentally on the Earth's built-in metronome. The metronome takes the form of astronomically driven Milankovitch-type variations in Earth's insolation. Changes in Earth's insolation quantities are indirectly recorded in the sedimentary archive after having passed through the filtering system of Earth's climate machine. Unlike radioisotopic dating methods, the observation of astronomically driven sedimentary cycles offers similar precision during the Paleogene as in the Neogene. Potentially, relative dating errors can be as small as a single astronomical cycle, e.g., 22, 41, 120 or 405 ka [*Laskar*, 1999].

[4] High-resolution age models are not only necessary to estimate geological rates of processes, but can also be used to extract information about the climate system and underlying astronomical variations [*Shackleton*, 2000; *Pälike and Shackleton*, 2000; *Pälike et al.*, 2004; *Billups et al.*, 2004; *Wade and Pälike*, 2004; *Raffi et al.*, 2006; *Pälike et al.*, 2006a, 2006b]. Invoking astronomical insolation cycles to explain ice ages was advanced by *Milankovitch* [1941], who argued that summer insolation in high northern latitudes is the controlling factor for ice sheet advance and retreat. Milankovitch postulated that if summer insolation values remain low enough, temperatures are also low, and prevent the significant melting of ice during summer. At present, the majority of authors who use insolation calculations still use the 65°N summer insolation as the forcing function, although modifications to this theory have now been proposed [*Huybers*, 2006]. High-resolution age models generated from sediment cores at extremely high latitudes, such as those recovered during Arctic Coring Expedition (ACEX) [*Backman et al.*, 2006; *Moran et al.*, 2006], offer the opportunity to test the sensitivity of local climatic forcing as a function of latitude.

[5] The analysis of climatic cycles, responding to insolation forcing, typically requires continuous, long and high-resolution records. Additional age control from biostratigraphy or magnetostratigraphy is required to provide anchoring points in the nearly repetitive pattern of Earth's insolation. This additional control is also necessary to determine which of the three contributors to insolation variations (climatic precession, obliquity, short and long eccentricity) are dominant in any given measured parameter.

[6] In the case of the ACEX record, these requirements are only partially met, as stratigraphic sections below the top few tens of meters are not fully recovered, and age control is mostly provided by relatively low-resolution

[1]National Oceanography Centre, University of Southampton, Southampton, UK.
[2]Graduate School of Oceanography, University of Rhode Island, Narragansett, Rhode Island, USA.
[3]Geophysics and Planetology, CEREGE, CNRS, University of Aix-Marseille 3, Aix-en-Provence, France.

Copyright 2008 by the American Geophysical Union.
0883-8305/08/2007PA001490

biostratigraphy. Thus, the same factors that make it difficult to achieve a high resolution and an accurate age model in the ACEX cores also hinder their cyclostratigraphic analysis. Nevertheless, the physical properties measured from the ACEX cores [*Backman et al.*, 2006; *Moran et al.*, 2006], as well as additional high-resolution data (organic carbon contents [*Stein et al.*, 2006], X-ray fluorescence (XRF) core scanner elemental concentrations [*Backman et al.*, 2006; *Spofforth et al.*, 2008], and biological proxies [*Sangiorgi et al.*, 2008b]), show a striking cyclical pattern during certain intervals on decimeter to meter scales. We exploit these cyclical variations in high-resolution measurements (1) to estimate relative sedimentation rates through several time slices where recovery was good, and (2) to derive a better understanding of what, if any, cyclicity is recorded in the unusual environments of the Arctic Ocean. Work by other authors has shown that climatic forcing can be represented through proxy records in the Arctic through several mechanisms, including variations of sea ice extent and intensity [*Krylov et al.*, 2008], variations in productivity and anoxic or suboxic preservation [*Stein et al.*, 2006; *Sangiorgi et al.*, 2008a], variations in terrigenous input [*Spofforth et al.*, 2008], variations in freshwater supply [*Sangiorgi et al.*, 2008a], and a close relationship between sediment properties (color, density, grain size) with climatic state [*O'Regan et al.*, 2008].

2. Materials and Methods

2.1. Physical Property Measurements

[7] As part of our analysis, we made use of the following physical property parameters measured during the onshore and offshore phase of ACEX [*Backman et al.*, 2006]. The main multisensor core-logger (MSCL) measurements obtained from the unsplit cores include gamma ray absorption bulk density (GRA), low-field (0.1 mT) volume magnetic susceptibility (MS) using two loops with offset frequencies of 621 Hz and 513 Hz with measurements adjusted to the standard 565 Hz response [*Backman et al.*, 2006], compressional wave velocity (PWL) and natural gamma ray (NGR) emissions [*Backman et al.*, 2006; *Blum*, 1997]. The sample resolution ranges between 2 to 5 cm between samples. For color reflectance (L*, b*) [*Blum*, 1997] the sampling interval is every 5 cm. Technically, we make use of the "spliced" section, however, in reality there is almost no overlap between cores below the top few tens of meters. We use the meters composite depth (mcd) scale [*Backman et al.*, 2006] to assign different nonoverlapping depths to different cores. A revised composite depth scale is now available for the upper tens of meters [*O'Regan et al.*, 2008], which is important to interpret beryllium-10 derived ages [*Frank et al.*, 2008; *Backman et al.*, 2008], magnetostratigraphic interpretations and high-resolution studies of Plio-Pleistocene sediments, but does not influence our analysis or interpretation.

2.2. X-Ray Fluorescence Measurements

[8] The multisensor track measurements obtained from the ACEX cores allow assessment of cyclical patterns in sediment density, mineralogical and grain size composition, and color. However, the ACEX core quality was compromised by the use of an extended core barrel–type recovery system [*Backman et al.*, 2006]. This system can result in partially filled core liners, or biscuiting, problems that are generally avoided when using a hydraulic piston coring system. A significant help in understanding whether the MSCL data patterns are due to variations of sediment properties, or due to drilling disturbances, is provided through the high-resolution measurement of (relative) major element fluctuations, measured on the surface of split archive halves. The detailed description of measurement techniques, calibration of XRF counts per seconds to absolute concentrations, and an evaluation of correlation between the elements (K, Ca, Fe, Al, Si, S, Mn, Ti) is given by *Spofforth et al.* [2008] (see also *Sangiorgi et al.* [2008b]). These measurements are shown to be useful to ascertain the relative contributions from terrigenous and biogenic matter to the bulk sediment.

[9] *Spofforth et al.* [2008] also generated a calibration of elemental concentrations to allow the conversion of raw XRF counts to calibrated concentrations. Similar to previous work, this analysis uses elemental concentration variations and physical property measurements as a semiquantitative geochemical approach to decipher sedimentary patterns [*Wehausen and Brumsack*, 1999; *Lourens et al.*, 2001; *Pälike et al.*, 2001]. The sampling resolution for calibration measurements (via ICP-AES) from subsections of the record was chosen on the basis of the shipboard age model [*Backman et al.*, 2006], aiming for a resolution in time of about 1 ka, and resulting in actual sampling intervals of between 0.5 cm and 2 cm [*Spofforth et al.*, 2008].

2.3. Other Measurements and Proxies

[10] Owing to the often noisy nature of the MSCL measurements obtained from the short XCB ACEX cores, it has proven difficult to obtain meaningful estimates for sedimentary patterns from just one single parameter. For this reason one of the approaches we chose here is to consider multiple proxy measurements simultaneously, using an algorithmic approach. Additional data sets that were generated as part of the ACEX effort include measurements on bulk organic carbon from the organic rich units 1/6 and 2, mostly from the Paleogene [*Stein et al.*, 2006] as well as isothermal remanent magnetization (IRM) and anhysteretic remanent magnetization (ARM) magnetic proxies produced for the Paleogene as part of the onshore standard measurement program (J. Gattacceca, unpublished data, 2006). All magnetization measurements were performed on U-channel samples (150 cm length, 2 cm by 2 cm cross section) using a 2G DC SQUID magnetometer. Measurement intervals were 2 cm. The field strength resolution is about 10^{-6} A m^{-1}. ARM was measured after imparting a 100 μT field, superimposed with a 100 mT alternating field. IRM was measured after imparting a field of 1000 mT. The full data set also includes field intensities after demagnetization with alternating fields of 50 mT (peak value). Magnetic proxy data (ARM/IRM ratio) were considered separately by *O'Regan et al.* [2008] for an evaluation of the Quaternary part of the ACEX record. Summary Figure 1 includes the

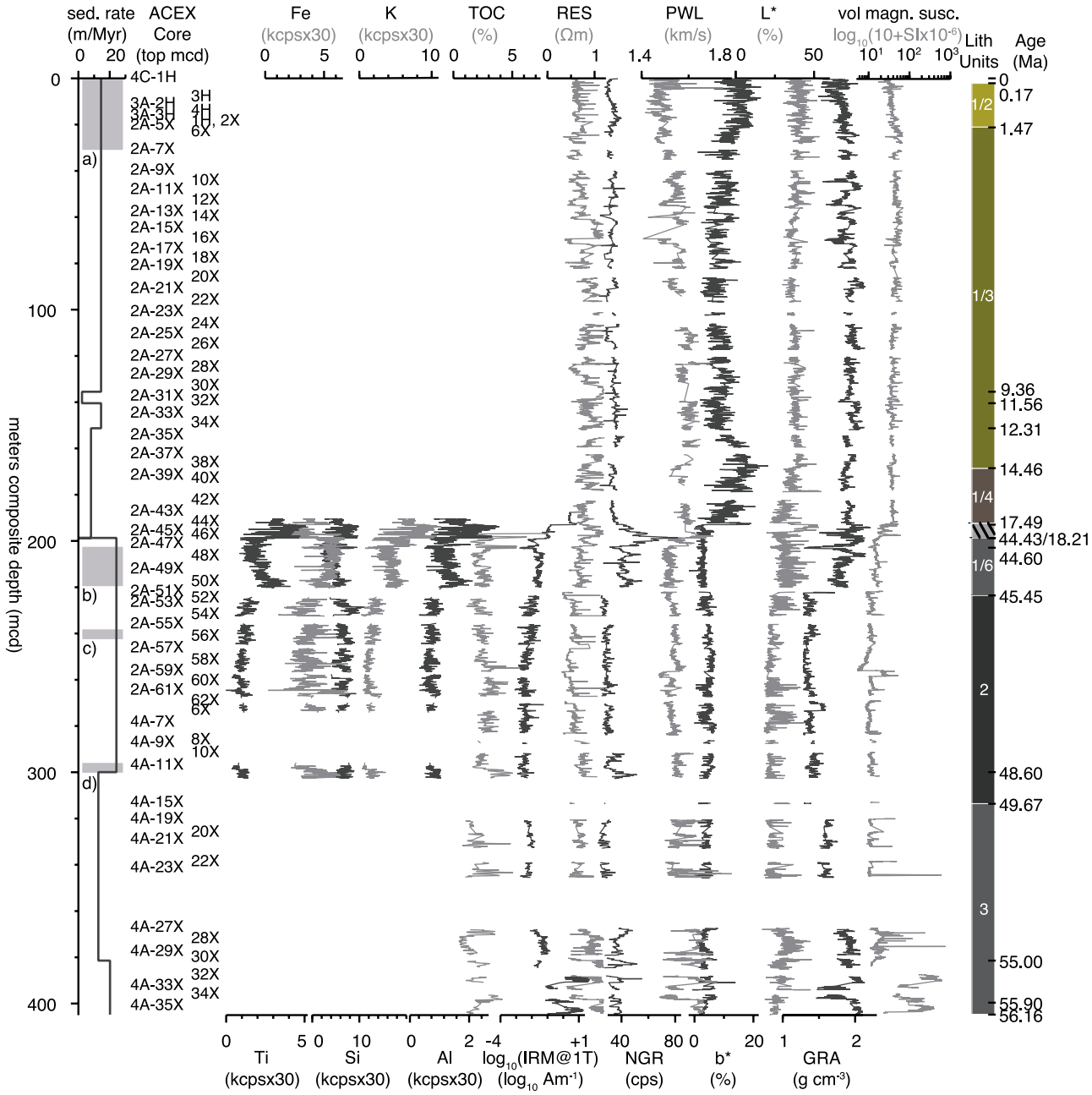

Figure 1. Summary plot of data used. (left) Meters composite depths (mcd) and cores used in splice together with the (right) sedimentation rates that result from the age model of *Backman et al.* [2008] (with lithological units [*Backman et al.*, 2006]). Data plotted are XRF-derived elemental concentrations of Ti, Fe, Si, K, and Al (in 1000 counts per second (cps)); organic carbon contents (TOC) [*Stein et al.*, 2006]; log isothermal remanent magnetization (IRM) at 1000 mT (in A m^{-1}); and multisensor track properties electrical resistivity (RES) (Ω m), natural gamma ray (NGR) (gamma counts s^{-1}), compressional wave velocity (PWL) (sound velocity, km s^{-1}), b* and L* (color reflectance, percent), gamma ray absorption (GRA) (bulk density, g cm^{-3}), and volume specific magnetic susceptibility ($\log_{10}$(instrument units $+10^{-6}$ International System of Units)). Grey shaded intervals labeled a, b, c, and d represent snapshot intervals analyzed in detail in this study.

sedimentation rates predicted using the age model of *Backman et al.* [2008].

2.4. Data Cleaning Procedures

[11] A first and necessary step before attempting frequency analysis of time series from sediment cores often involves the preparation and pruning of existing data sets, so as to avoid spurious spikes in the records and to enhance the signal-to-noise ratio prior to analysis. Outliers originating from end-of-core effects (e.g., end caps, partially filled core liner at the end of cores or sections) were readily identified visually, and typically were removed prior to spectral analysis. For some measurements (e.g., IRM) we applied an algorithmic spike reduction, by filtering out all those points that lie outside the 1.5 one-sided standard deviation from the median over 5 running points. This step was successful in eliminating anomalous spikes in the records. In the case of the ACEX cores, several spikes, particularly in the bulk density record, were not the result of core disturbances, but instead resulted from the occurrence of both drop stones and pyrite nodules in the records. While drop stones and pyrite nodule occurrence may be partially driven by climatic variations, they do not appear to linearly scale with a climatic forcing signal, and are thus not analyzed here. We attempted to manually remove such spikes prior to analysis. All records were resampled to an equal depth step (while preserving the highest sample resolution within a given record), linearly detrended, and normalized by subtracting the arithmetic mean and dividing by the standard deviation [*Weedon*, 2003].

2.5. Frequency Ratio Snapshots

[12] In order to establish whether the ACEX physical property and XRF records are compatible with a hypothesis that invokes orbital forcing to explain the cyclical patterns observed, several analytical approaches are possible. One approach we use is to take subsections from the entire data set, spanning one or two cores with the highest-quality measurements, and compute an average power spectrum, using the multitaper method [*Ghil et al.*, 2002]. Calculated spectra then enable us to apply a frequency ratio test between significant peaks. Here we do not match the core data to astronomical templates using available biostratigraphy and magnetostratigraphy, but instead analyze the frequency ratio of the cycles that are preserved and assume that the ratio of dominant sedimentary cycle frequencies should follow the pattern predicted by astronomy (roughly 400 ka: 120 ka: 41 ka: 22 ka ratios). This method, which is suitable for uncertain age control, has been applied previously [*Hilgen*, 1991; *Dinarès-Turell et al.*, 2003; *Raffi et al.*, 2005], and allows a rough estimate of likely sedimentation rates if Milankovitch frequencies at the predicted ratio are present in the snapshots of cores analyzed.

2.6. Wavelet Analysis

[13] We run time-evolutive spectral analyses in the depth domain to establish the presence of orbital signals [*Weedon*, 2003]. We apply a continuous wavelet transform [*Torrence and Compo*, 1998] (online software available from http://atoc.colorado.edu/research/wavelets/, accessed 29 April 2007) in order to establish how the spectral power of proxy series vary with depth. This method requires interpolation of our series to equal depth steps, which were chosen to preserve the maximum depth resolution across the records (typically 2 cm intervals). We show here the results from the entire stratigraphic interval recovered in the case of the physical property data (0 to 404.68 mcd) (Figure 2), and over a short interval for units 1/6 and 2 for selected XRF measurements [*Spofforth et al.*, 2008], organic carbon contents [*Stein et al.*, 2006], and IRM (Figure 3).

[14] We converted the astronomically calculated [*Laskar et al.*, 2004] insolation at 85°N for June–July from an absolute timescale to the composite depth scale (mcd), using a reverse linear interpolation from the age model of *Backman et al.* [2008]. This allowed a comparison of predicted orbital cycle frequencies in the depth domain to those obtained from the proxy series (Figure 2). We note that insolation quantities are typically dominated by obliquity and precession, and that geological records often show a red background noise, muting the higher frequencies [*Weedon*, 2003; *Pälike et al.*, 2006a]. We also calculate the predicted position of the four main Milankovitch bands (405, 110, 41, 22 ka) using the simple linear age model of *Backman et al.* [2008]. We use the predictions from this linear age model as a visual aid to establish where in the frequency-depth continuum one would expect to see orbitally controlled cyclical patterns. This approach made the double assumption that the sedimentation rates of *Backman et al.* [2008] are correct and that records are potentially astronomically forced.

2.7. Multichannel Singular Spectrum Analysis

[15] If several proxy measurements exist for the same depth interval, it is necessary to reconcile the different information contained in each series. The availability of multiple data sets should allow the enhancement of the signal-to-noise ratio of a common encoded signal. Each proxy curve is a mixture of a climatological signal, noise, and nonperiod changes that are common to all data series because of local geological conditions. "Noise" in proxy curves reflects measurement, calibration, or sedimentological uncertainties. It is unpractical to analyze all data series separately, and thus a useful approach is to apply analysis to a combination curve of all measurements available.

[16] To achieve a decomposition into correlated signals and noncorrelated signals (noise), we have applied an approach previously developed for meteorological data sets, namely singular spectral analysis (SSA) decomposition [*Vautard and Ghil*, 1989; *Vautard et al.*, 1992]. Here we used an extended method (multichannel singular spectrum analysis (MSSA)) that can be applied to multiple proxy channels [*Plaut and Vautard*, 1994; *Jiang et al.*, 1995]. This approach allows us, without a priori knowledge, (1) to extract a subset of oscillations that is common to all proxy series considered, (2) to establish which are the dominant periodicities, and (3) to reconstruct the higher-order principal components identified in item 2, thus enhancing the signal-to-noise ratio. We ran several experiments using the MSSA approach to first identify those components that show correlated oscillations for depth intervals labeled

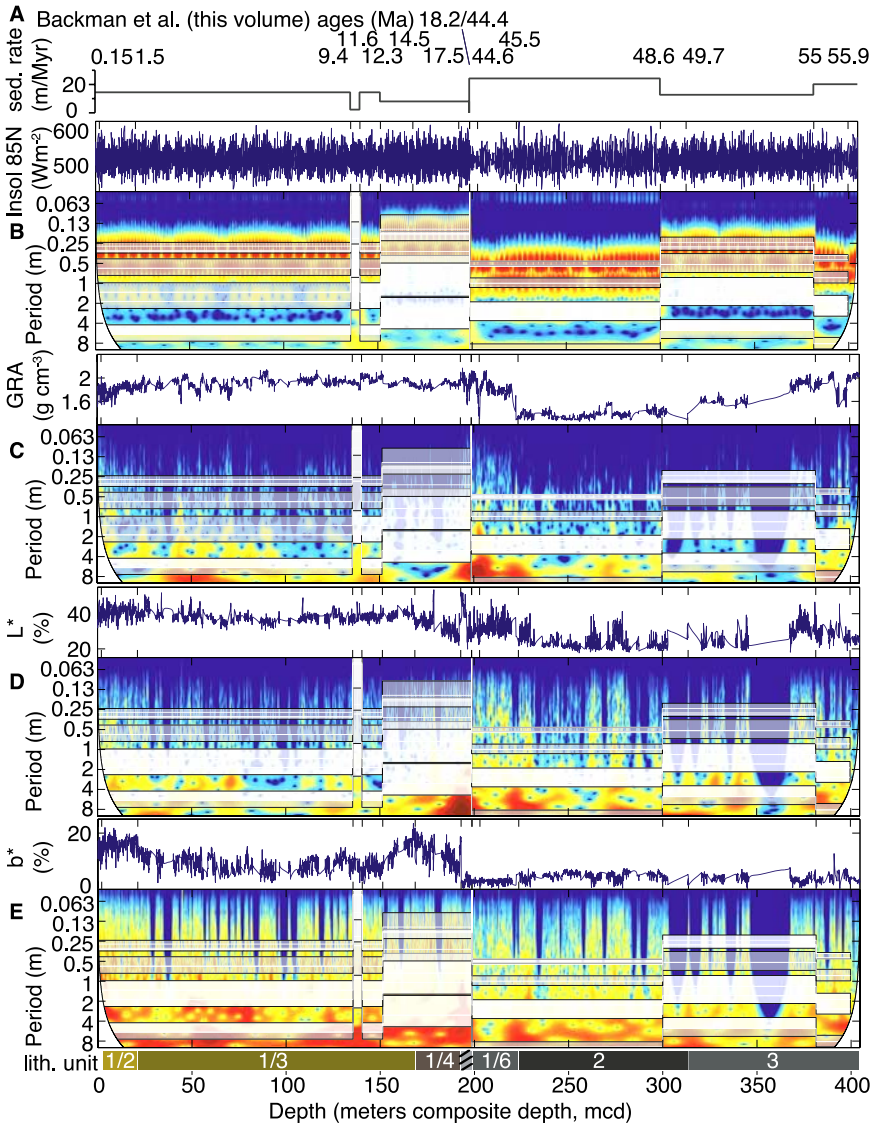

Figure 2. Continuous wavelet transform (CWT) analysis [*Torrence and Compo*, 1998] of data in depth domain (entire record). (a) Ages and apparent sedimentation rates of *Backman et al.* [2008]. Note major hiatus between ~18 and 44 Ma [*Sangiorgi et al.*, 2008a]. (b) CWT analysis of insolation calculated at 85°N for June–July [*Laskar et al.*, 2004] after remapping to depth using age model from Figure 2a. Superimposed are white shaded bands that indicate the predicted position of 22, 41, 110, and 405 ka Milankovitch bands. (c–e) CWT analyzed for physical property data bulk density (GRA), lightness (L*), and yellow-blue (b*) [*Backman et al.*, 2006]. Sedimentary units and meters composite depths (mcd) are indicated below. Curved white edges indicate typical shape of "cone of influence," where edge effects influence the spectra. Similar shapes would extend around each core gap (not plotted).

"b" and "c" in Figure 1, and then reconstructing selected principal components that show strong and stable common oscillations between the proxies considered.

3. Results

[17] In section 3.1 we present sedimentation rates for snapshot depth intervals from the ACEX record, indicated by a–d in Figure 1. We apply this strategy because of the large number of core gaps across the record, which make a continuous analysis not possible. We compared the derived sedimentation rate from each snapshot interval with the integrated age model of *Backman et al.* [2008].

3.1. Pleistocene Sedimentation Rates: 0–27 mcd

[18] A detailed analysis of rock magnetic properties and physical proxies resulted in a new high-resolution age model for the Pleistocene ACEX section, and is presented fully by *O'Regan et al.* [2008]. The depth interval covered in that study is indicated by "a" in Figure 1. *O'Regan et al.* [2008] exploited characteristic patterns in the proxy data to allow correlation with existing records and ages. They also

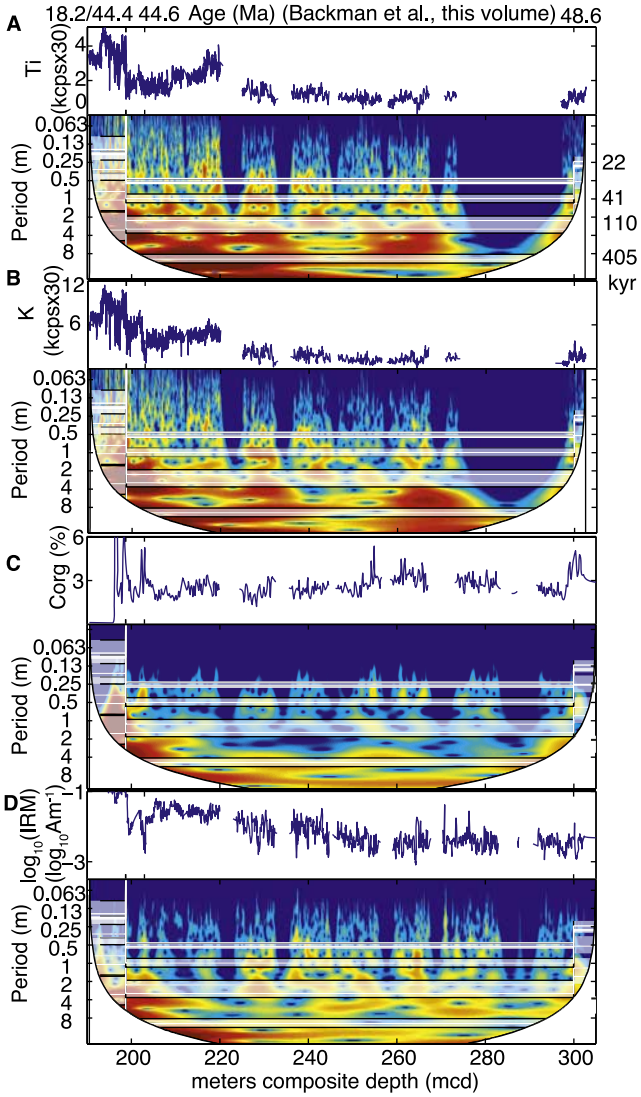

Figure 3. CWT analyses as in Figure 2 but for depth interval 190–300 mcd (bottom of sedimentary unit 1/4 through base of unit 2) for (a) XRF-derived Ti counts, (b) K counts, (c) organic carbon TOC, and (d) log(IRM).

used a cyclostratigraphic approach to constrain paleomagnetic interpretations back to the Cobb Mountain event (~1200 ka). The new high-resolution age model presented by *O'Regan et al.* [2008] results in sedimentation rates that are very similar to the average Neogene rates of about 1.45 ± 0.1 cm ka^{-1} obtained by ^{10}Be/^{9}Be analysis of *Frank et al.* [2008].

[19] Generally, the ages of *O'Regan et al.* [2008] confirm the overall high sedimentation rates around 10–20 m Ma^{-1} revised recently for the Arctic Ocean Basin [*Backman et al.*, 2004]. The wavelet spectra calculated in the depth domain for color reflectance (Figure 2e) confirm this finding by displaying consistent power around the periods predicted by the ^{10}Be/^{9}Be age model (periodicities around 0.25 m, 70 cm, and 1.5 m, corresponding to climatic precession, obliquity, and the short eccentricity frequency ratios). The continuous wavelet transform analysis of physical properties (Figure 2) indicates that sedimentation rates estimated from frequency ratios of sedimentary cycles remain largely compatible with the ^{10}Be/^{9}Be–derived age model, but possibly indicating marginally smaller sedimentation rates around 100 mcd.

3.2. Paleogene Sedimentation Rates: 200–404.8 mcd, ~44–56.2 Ma

[20] The following three snapshots were selected from lithological units 1/6 and 2 from the ACEX record, below a major hiatus separating the Miocene from the middle Eocene at 198.7 mcd [*Sangiorgi et al.*, 2008a; *Backman et al.*, 2008]. We note that this hiatus itself is well characterized in depth by the XRF measurements as a sharp break in elemental concentrations, with elevated counts just above this major >26 Ma lasting hiatus (Figure 3).

3.2.1. Sedimentary Unit 1/6 (Middle Eocene)

[21] Sedimentary units of the ACEX stratigraphic section discussed here, and shown in Figure 1, are defined by *Backman et al.* [2006]. Sedimentary unit 1/6 represents the youngest Paleogene material that was recovered during ACEX, just below a major hiatus [*Sangiorgi et al.*, 2008a]. The wavelet analysis of this interval (Figures 2 and 3) indicates that several sedimentation rates result in cycle periods that show frequency ratios compatible with orbital forcing. These sedimentation rates were variable across this unit. For the interval between 203 and 220 mcd within unit 1/6 (marked as "b" in Figure 1), the physical properties, the XRF-derived elemental concentrations and calibrations [*Spofforth et al.*, 2008], the organic carbon content [*Stein et al.*, 2006] and the isothermal remanent magnetization (IRM) all show a pronounced cyclicity. The cycle period ranges from a short ~15 cm spacing to longer decimeter and meter scales (Figures 3 and 4), with strong correlations between the different parameters. We make use of the MSSA decomposition technique to isolate the largest amplitude oscillations that are common to all proxies. Figure 4 shows an example of this method, where the raw records are input into the MSSA algorithm, computed with 200 lags for an interpolated sample spacing of 0.5 cm, and computing 40 principal components. The strongest and most coherent oscillations are then selected, and used to reconstruct a new signal with a higher signal-to-noise ratio. This reconstructed and "cleaned" signal explains about 42% of the total variance across all XRF parameters. We investigate the spectral characteristics of individual reconstructed components in more detail (Figure 5). The amplitude normalized spectral peaks of individual reconstructed components occur at frequencies at around 2–4 cycles m^{-1} and 6–8 cycles m^{-1}. Some components show peaks at both frequency ranges (e.g., principal reconstructed components (PCRCs) 12 and 13), and band-pass filtering of the raw series indicate the higher-frequency oscillations are not harmonics, but real oscillations.

[22] Figure 6a shows the XRF results from this interval in detail, and illustrates the observation that all records correlate extremely well with each other within this unit (decreases in Fe correspond to increases in Ti, Al, Si). The cycle spacing in this interval is also variable: between

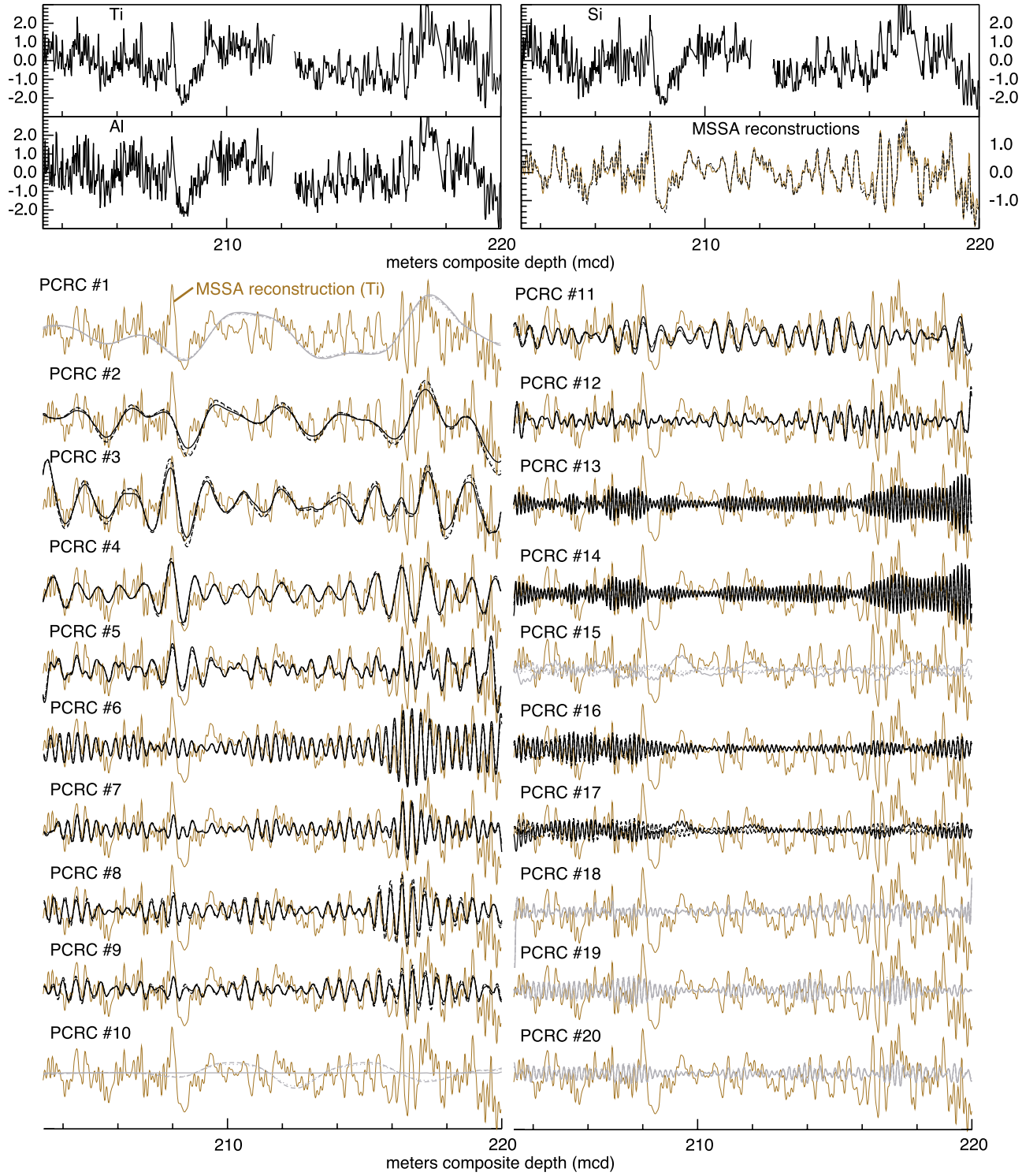

Figure 4. Unit 1/6 analysis, shown in Figure 1 as "b." (top) XRF-derived Ti, Al, and Si counts, normalized to standard deviation, with multichannel singular spectrum analysis (MSSA) reconstructions from the reconstructed principal components shown below. There is one reconstructed principal component per element (Ti, solid; Al, dashed; and Si, dotted). Grey components were not used for reconstruction (they do not pass the paired frequency test [*Ghil et al.*, 2002]). Small-amplitude principal reconstructed components (PCRCs) 21–40 were also not used or plotted. The reconstructed components of the proxy series combined from Al, Si, Fe, and Ti explain about 42% of the total variance. (bottom) Reconstructed Ti for each reconstructed principal component for comparison (orange).

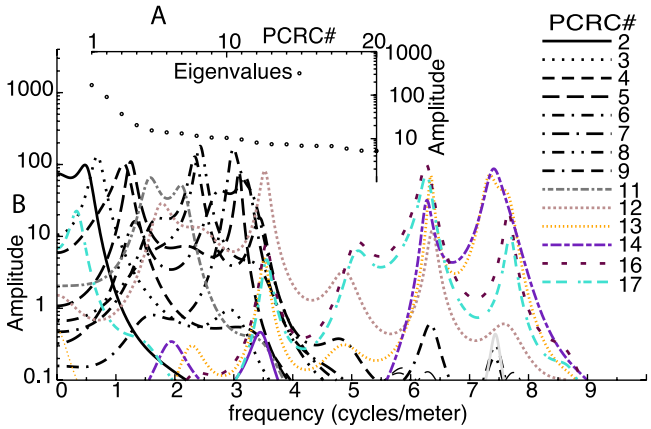

Figure 5. Spectral analysis of MSSA reconstruction principal components. (a) Amplitude-sorted eigenvalues for each PCRC of Figure 4 on a logarithmic amplitude scale. (b) Maximum entropy spectrum [*Press et al.*, 1992] for each PCRC of Figure 4.

206 and 208 mcd cycles are more closely spaced. From 210 to 216 mcd their amplitude is reduced, and explained by a core gap. Between 216 and 220 mcd, the amplitude of individual cycles is higher than in other intervals.

[23] A Blackman-Tukey spectral analysis [*Tukey*, 1977] of the signal reconstruction from this interval (Figure 6b) identified several spectral peaks, where the high-frequency component oscillates between 6 and 8 cycles per meter (~15 cm spacing), and the lower-frequency components are split with periods around 33 cm, 70 cm and 2 m. Figure 6b illustrates the frequency ratio approach used to identify two possible sedimentation rate hypotheses. We make use of a template of predicted astronomical frequencies (in cycles per meter) as a function of sedimentation rate for climatic precession (22 ka), obliquity (41 ka), and short (~110 ka) and long (405 ka) eccentricity. Identifying the 33 cm spaced oscillations as climatic precession frequencies yields model 1, with sedimentation rates between 10 and 20 m Ma^{-1}, which is compatible with the position of the lower frequency peaks identified. Alternatively, if the 15-cm scale cycles are interpreted as precession-driven, a different hypothesis (model 2) is possible, with resulting sedimentation rates of

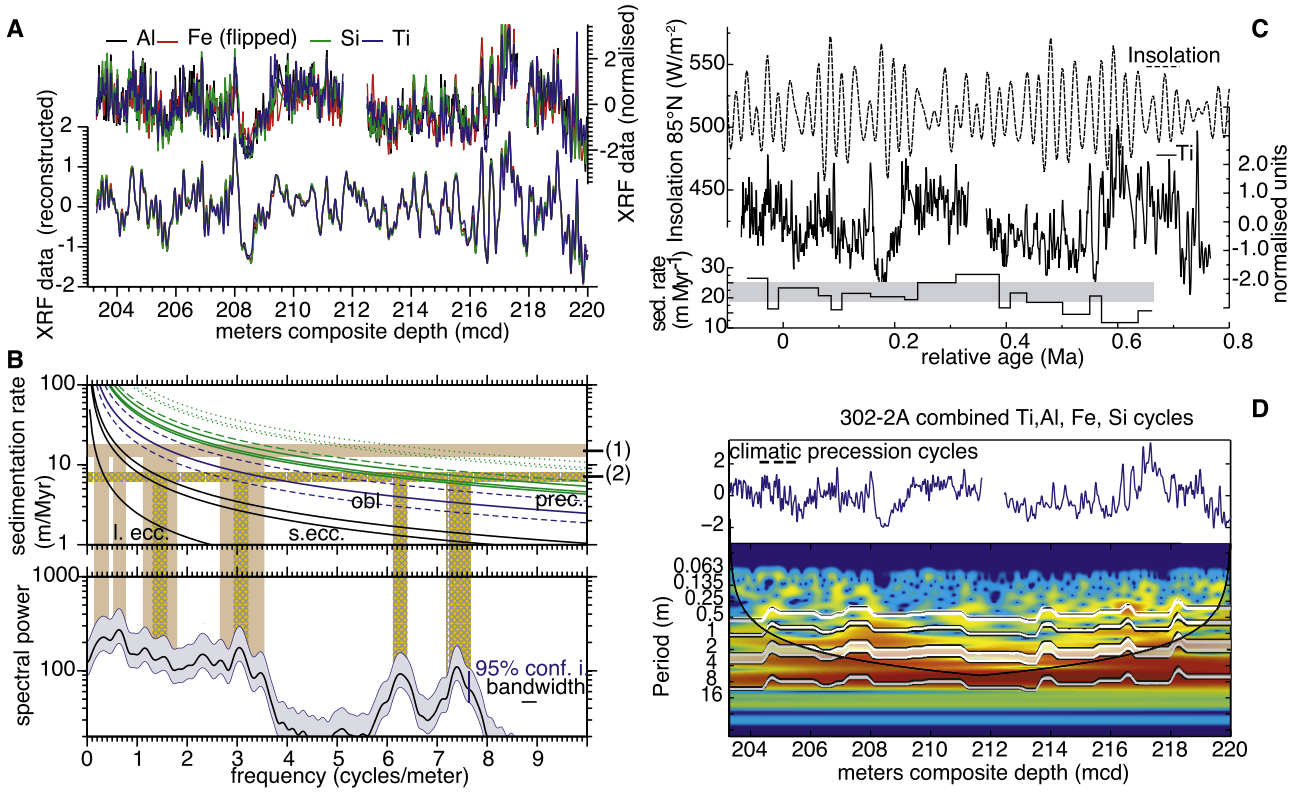

Figure 6. Unit 1/6 analysis, shown as "b" in Figure 1. (a) XRF data normalized to standard deviation and MSSA reconstruction of significant principal components. Al, Si, and Ti anticorrelate with Fe. (b) Blackman-Tukey spectral analysis of reconstruction from Figure 6a (bottom plot, with 95% confidence interval and bandwidth indicated), with two interpretations of frequency ratios labeled 1 and 2 if identifying spectral peaks with predicted position of Milankovitch bands as a function of sedimentation rate (top plot). (c) Relative timescale developed for Ti record using frequency ratio labeled 1 in Figure 6b. (d) Wavelet analysis of Ti combined cycles against depth, with superimposed Milankovitch bands using age model from Figure 6c.

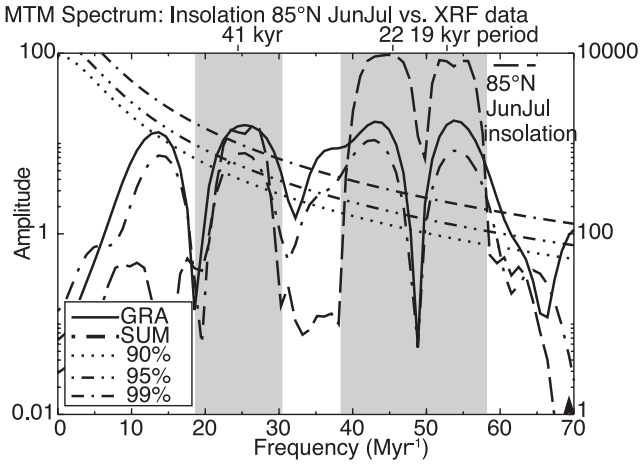

Figure 7. Interval "c" in Figure 1, modified from *Sangiorgi et al.* [2008b]. Multitaper spectral analysis of insolation, GRA bulk density, and summary signal extracted by MSSA from combined bulk density, magnetic susceptibility, XRF-derived Ti, Al, and K, and natural gamma measurements.

around 6 to 8 m Ma^{-1}. We note here that there is abundant pyrite present within this unit, possibly influencing the high-frequency, high-amplitude oscillations. At present, we cannot make a definite choice as to whether model 1 or 2 is the correct one, based on spectral arguments alone. However, we prefer model 1, which is compatible with other sedimentation rate constraints [*Backman et al.*, 2008]. However, hypothesis 1 implies that the higher-frequency component with a cycle spacing of 15 cm represents half-precession cycles, which is not likely given that these are predicted to occur near the tropics only [*Berger and Loutre*, 1997]. The MSSA decomposition shows that the high-frequency oscillations of the XRF records occur in the upper (204–208 mcd) and lower intervals (217–220 mcd) of lithological subunit 1/6. As both sedimentation rate models 1 and 2 are compatible with frequency ratios predicted by astronomy (with frequency ratios of 3:1.5:0.5 cycles m^{-1} for model 1, or 7:3:1.5 for model 2), it is not possible, at present, to come to a definite conclusion. One possibility that reconciles both models are variations of sedimentation rate within the interval studied by a factor of 2. This factor is common in geological records [e.g., *Pälike et al.*, 2006b], and are also supported by a good match between insolation target and data after a tentative tuning of the records to insolation calculations (Figure 6c).

[24] Figure 6c shows how the sedimentation rate model 1 can be used to derive a relative ("floating") age scale by comparison of the XRF elemental variations with computed insolation curves from *Laskar et al.* [2004]. Also shown are sedimentation rates from this rudimentary "tuning," again yielding linear sedimentation rates of between 10 and 25 m Ma^{-1}. These show a visual match between predicted Milankovitch bands and high-amplitude "ridges" in the wavelet spectrum (Figure 6d). Hence, for unit 1/6 we find that the biostratigraphic age control is compatible with the cycle spacing observed, but there is also a different possible sedimentation rate model that is ~50% slower than that predicted from existing age control [*Backman et al.*, 2008].

3.2.2. Sedimentary Unit 2 (Eocene), Core 2A-55X

[25] We now extend our analysis to an interval from sedimentary unit 2, which is also characterized by high-amplitude and coherent oscillations in XRF and physical properties, and for which an additional set of biological proxies were generated [*Sangiorgi et al.*, 2008b]. This interval is marked by "c" in Figure 1 and encompasses core 2A-55X, from about 236 to 241 mcd.

[26] A detailed analysis of available measurements from this core is presented by *Sangiorgi et al.* [2008b]. The wavelet analysis in Figure 3 suggests that the sedimentation rates of about 20 m Ma^{-1} derived for Core 2A-55X within unit 2 can be extrapolated downward to at least 270 mcd, based on the horizontal "ridges" in the wavelet spectra that illustrate the presence of oscillations at the main periods around 50 cm and 1 m.

[27] Applying a light "tuning" to the records from Core 2A-55X and calculating a multitaper power spectrum from this tuned record (Figure 7) [see also *Sangiorgi et al.*, 2008b, Figure 9] illustrates that the amplitude ratio of the obliquity and climatic precession signal in the XRF and physical properties is about 1:1, which has important ramifications for insolation models, illustrated in section 4.

3.2.3. Sedimentary Unit 2 (Eocene), Core 4A-11X

[28] The interval around 300 mcd was very sparsely recovered during ACEX, but yielded a relatively complete Core 4A-11X which showed a remarkable record of *Azolla* fern spores within unit 2 [*Brinkhuis et al.*, 2006].

[29] Wavelet analysis for this interval (Figures 2 and 3) indicates that the sedimentation rate in this crucial interval was also near 20 m Ma^{-1}, and that the predicted decrease in sedimentation rate down core [*Backman et al.*, 2008] in most likelihood occurred below core 302-4A-11X.

4. Discussion

4.1. Sea Ice and Orbital Insolation

[30] Results from analyzing the Eocene ACEX time series needs wider consideration of likely effects of orbital forcing on climate processes in the high latitudes. The variation of elemental concentrations [*Backman et al.*, 2006; *Spofforth et al.*, 2008] and biological proxies [*Sangiorgi et al.*, 2008b] suggests a potential role of sea ice variations in response to orbital forcing. The presence of sea ice in the Arctic plays an important role in interactions between insolation forcing and climatic response, for example, through the albedo-temperature positive feedback. It also controls exchange of heat between the ocean and the atmosphere, and is implicated in variations of the thermohaline circulation intensity.

[31] Recently several modeling studies [*Gallimore and Kutzbach*, 1995; *Jackson and Broccoli*, 2003; *Tuenter et al.*, 2005] have investigated the response and role of sea ice in the Northern Hemisphere in response to orbital insolation changes. *DeConto et al.* [2007] investigated the feedback of sea ice on climate on Antarctica. The high latitudes experience large-amplitude variations in orbital insolation on annual and Milankovitch timescales (tens of thousands to

hundreds of thousands of years). A data set from the Arctic can provide a first test of the predictions arising from these modeling studies.

[32] *Gallimore and Kutzbach* [1995] used a low-resolution general circulation model with extreme orbital configurations to investigate how annual mean sea ice thickness and autumnal sea ice coverage change under different orbital configurations. They found that an increase in Earth's obliquity (tilt) by three degrees results in a decrease of mean sea ice thickness of 50%, and a reduced autumnal sea ice coverage by 41%. Under a different forcing experiment, using a relatively high eccentricity, and changing the time of Earth's closest approach to the sun (perihelion) from Northern Hemisphere (NH) summer to NH winter resulted in a 21% reduction in mean ice thickness, but no change in the autumnal sea ice coverage. The authors attribute the effect of larger obliquity on sea ice to enhanced annual mean radiation, and the precessional effect on seasonal interaction between those modeled processes that govern sea ice growth and melt, and the heat transfer through sea ice. For precession, a change from the date of perihelion from summer to winter results in a reduction of summer radiation in the northern extratropics of about 80 W m^{-2}, while for winter the changes are smaller because of the overall smaller radiation, and only reach about 20 W m^{-2} at 45°N latitude. In the case of the increased tilt, and combined increased tilt and summer perihelion experiments, the annual mean surface temperatures in the model study were almost 6°C higher over the high-latitude ocean area (60°–90°N), resulting in less sea ice cover. The authors also found a pronounced sensitivity of snow cover on the northern continents in response to changed orbital configurations. *Gallimore and Kutzbach* [1995] investigated the sea ice and snow response to insolation changes using extreme values for the past 115 ka. They acknowledge that their sea ice formulation ignores the effects of ice dynamics, leads, multilayer heat conduction, brine pockets, and snow accumulation on top of the ice, as well as the level of atmospheric CO_2 concentrations, which are likely to have been very different for the Eocene time slices [*Pagani et al.*, 2005] we have analyzed from the ACEX records.

[33] In addition to the modeling result that obliquity and precession changes both have the potential to profoundly affect sea ice coverage and extent in the Northern Hemisphere, largely through changes in boreal summer insolation [*Gallimore and Kutzbach*, 1995; *Jackson and Broccoli*, 2003; *Tuenter et al.*, 2005] showed that an additional effect during high summer insolation is a reduction in the occurrence of rapid (sub-Milankovitch timescale) shifts in sea ice cover, as well as changes in the Atlantic thermohaline circulation.

[34] In contrast to the Northern Hemisphere insolation time series, which would predict a very strong forcing of high-latitude climate by climatic precession, climate proxy records show a large response of the global climate system on obliquity timescales, at least during the late Pliocene and early Pleistocene [e.g., *Tiedemann et al.*, 1994]. More recently, a new theory for insolation calculations was suggested [*Huybers*, 2006] to explain these observations from climate records. This theory uses integrated positive degree days instead of mean monthly insolation time series, resulting in time series that are dominated by obliquity instead of climatic precession. The positive degree days time series is clipped above a minimum threshold. The effect of this clipping is that with higher thresholds the obliquity amplitude in these new insolation records is reduced, and the amplitude of climatic precession is enhanced. It is thus possible to use observed ratios of obliquity to climatic precession amplitudes from climate records to obtain best fitting threshold values for positive degree day insolation calculations.

4.2. Insolation Forcing in the Arctic: ACEX Data

[35] It is interesting to note that despite poor core recovery and lack of overlapping cores that would allow the construction of a detailed "splice" the method applied here can still result in useful determinations of sedimentation rates, and constrain rates of change within the Cenozoic record from the Arctic Ocean. It was useful to analyze a large number of different proxy measurements, as any individual data series has a too low signal-to-noise ratio. Investigating several "snapshots" of Eocene time, the revised picture of sedimentation history within the Arctic Ocean [*Backman et al.*, 2004] demonstrates that it was not sediment starved throughout the Paleogene.

[36] Our analysis also allows us to provide information on dominant orbital forcing parameters on climate proxy records during the Eocene, specifically, the relative amplitude of obliquity versus climatic precession response. The correlation of proxy parameters in the Eocene part of the ACEX cores strongly suggests that higher elemental concentrations of Al, Ti and K (as derived by XRF), for example, are controlled by sea ice transport [*Sangiorgi et al.*, 2008b]. The identification of orbitally driven sedimentary cycles close to the geographic north pole is interesting, as it would allow the testing of several paradigm views that arose from the original Milankovitch theory.

[37] In particular there is still a large debate over why the orbital cycles recorded in ice and marine cores are not dominated by 41 ka and 21 ka cycles during the last several hundred thousand years, as insolation forcing would predict. Instead, records show ~100 ka spaced oscillations that have traditionally been explained as eccentricity cycles. However, several hypotheses have been put forward that explain the ~100 ka spacing as a set of noncomplete obliquity cycles, that stochastically appear every 80 or 120 ka [*Huybers and Wunsch*, 2005].

[38] Our records from ACEX allow us to explore the new prediction of *Huybers* [2006] and previous modeling studies [*Tuenter et al.*, 2005] by analyzing the relative amplitude ratio between obliquity and climatic precession cycles in our data. The model of *Huybers* [2006] allows the calculation of his new insolation time series, for a given latitude and for a set of cutoff insolation values. Figure 8a shows the predicted ratio of obliquity to precession amplitude in the local insolation forcing. Obliquity is by far overpowering the precession component in the local forcing for cutoff values higher than about 100 W m^{-2}.

[39] *Huybers* [2006] used a very strong global correlation between observed local air temperature, and local instanta-

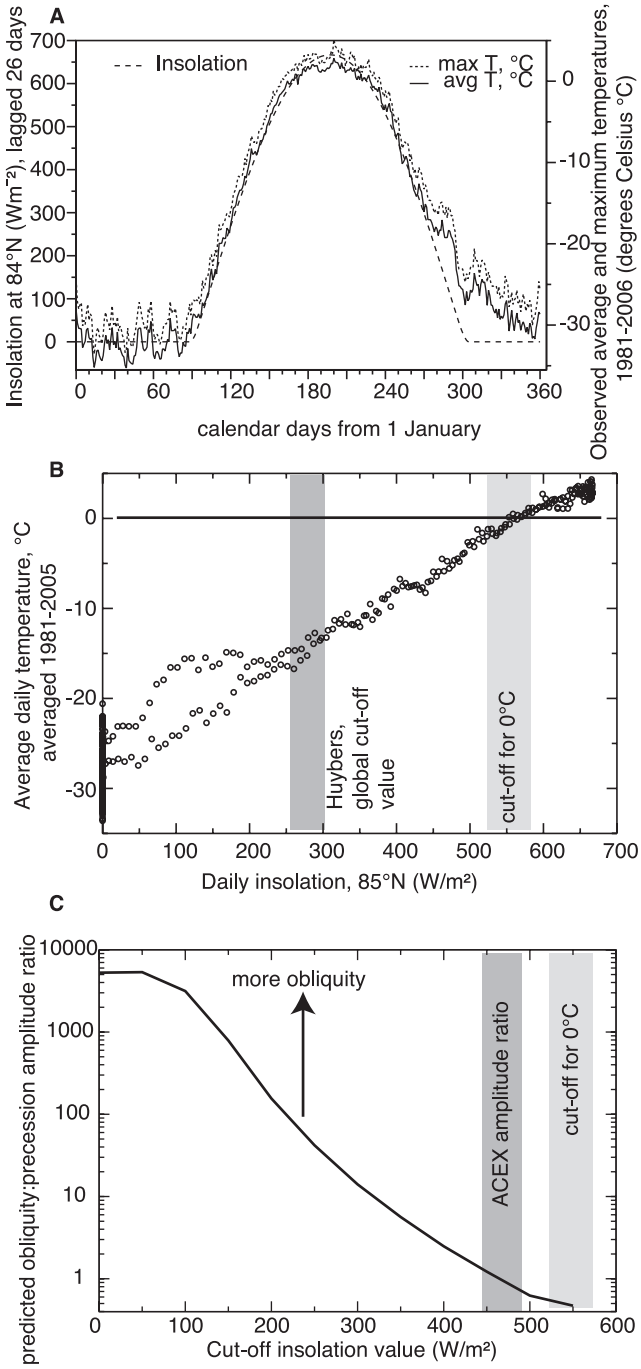

Figure 8. (a) Average and maximum daily temperature at weather station 04301 (~84°N), plotted from 1 January and averaged from 20 years of observation against local daily insolation, lagged by 26 calendar days. (b) Crossplot of lagged insolation and daily temperature from Figure 8a. (c) Amplitude ratio of obliquity:climatic precession from *Huybers* [2006] calculation as a function of cutoff insolation value, with amplitude ratio of near 1:1 from ACEX record marked (see Figure 7).

neous insolation lagged by 30 d, to make a prediction of what this cutoff point might be globally, and arrives at a value of about 250 W m^{-2}, resulting in a much reduced precession component in local forcing.

[40] In the case of the ACEX location, near the geographic north pole (87.5°N), and within the Arctic circle with constant daylight during summer and constant darkness during winter, we could expect a strong local forcing of sea ice formation, melting and transport in response to the local insolation forcing.

[41] We have applied the method of *Huybers* [2006] to investigate the predicted response of local temperature to insolation by comparing the temperature records from WMO weather station 04301 (Kap Morris Jesup, north Greenland, 83°39′N, 033°22′W), with insolation computed at 85°N (Figure 8). Figure 8a shows a strong correlation between calculated local insolation (lagged by 26 d, which provides the best fit) and observed daily temperatures. Figure 8b illustrates that the cutoff insolation value for average daily temperatures above 0°C is about 550 W m^{-2}. In Figure 8c, this cutoff value would predict a local insolation forcing that is dominated by precession with an amplitude ratio of obliquity versus climatic precession of about 1:10, which might be taken as the temperature most sensitive for the melting of sea ice.

[42] In the ACEX records, however, we establish an amplitude ratio closer to 1 (Figure 7). While these results indicate that the amplitude ratio of obliquity to climatic precession, predicted from the present-day transfer function of local insolation to temperature, does not directly apply to the Eocene time series, we nevertheless find that the methodology used by *Huybers* [2006] would predict cutoff insolation values for the Arctic (550 W m^{-2}) that are not very different to those suggested by the amplitude spectra calculated from the ACEX values (450–500 W m^{-2}). We therefore conclude that the methodology of *Huybers* [2006] warrants further investigation, and comparison with data records from other latitudes and time slices. Our results are also compatible with the influence of obliquity and climatic precession established through modeling studies for the past glacial cycle [*Gallimore and Kutzbach*, 1995; *Jackson and Broccoli*, 2003; *Tuenter et al.*, 2005].

5. Summary and Conclusions

[43] In summary, we evaluate the nature of oscillations in physical proxy measurements and XRF-derived elemental concentrations from the Arctic Ocean during snapshots of the Cenozoic. Even though the stratigraphic recovery is incomplete, advanced time series analysis methods allow us to put additional constraints on sedimentation rates during the Eocene. The determined sedimentation rate options are always compatible with those predicted by lower-resolution biostratigraphic control, and yield sedimentation rates of the order of 10–20 m Ma^{-1}. We establish that recent revised methods of insolation calculations are useful to make quantitative comparisons between the data recovered during ACEX, and predicted behavior of insolation. The ACEX records show a ratio of orbital obliquity and climatic precession imprint that is close to 1:1, and would predict

an insolation cutoff value for *Huybers* [2006] positive degree day insolation calculation of about 450–500 W m^{-2}, close to the local very high-latitude value predicted theoretically (550 W m^{-2}).

[44] **Acknowledgments.** We are grateful to the expedition onshore and offshore science party, as well as the crews of the I/B *Oden*, I/B *Vidar Viking*, and I/B *Sovetsky Soyuz*. This research used samples provided by the Integrated Ocean Drilling Program (IODP). IODP is sponsored by the U.S. National Science Foundation and participating countries under the management of Joint Oceanographic Institutions, Inc. Financial support was provided by the Nuffield Foundation and the U.K. Natural Environment Research Council (NERC) (reference NE/D000343/1) to H.P. and by NERC studentship (reference NER/S/A/2005/13474) to D.J.A.S.

References

Backman, J., M. Jakobsson, R. Lovlie, L. Polyak, and L. A. Febo (2004), Is the central Arctic Ocean a sediment starved basin?, *Quat. Sci. Rev.*, *23*(1113), 1435–1454, doi:10.1016/j.quascirev.2003.12.005.

Backman, J., K. Moran, D. B. McInroy, L. A. Mayer, and the Expedition 302 Scientists (2006), *Arctic Coring Expedition (ACEX)*, *Proc. Integr. Ocean Drill. Program*, *302*.

Backman, J., et al. (2008), Age model and core-seismic integration for the Cenozoic Arctic Coring Expedition sediments from the Lomonosov Ridge, *Paleoceanography*, doi:10.1029/2007PA001476, in press.

Berger, A., and M. F. Loutre (1997), Intertropical latitudes and precessional and half-precessional cycles, *Science*, *278*, 1476–1478, doi:10.1126/science.278.5342.1476.

Billups, K., H. Pälike, J. E. T. Channell, J. C. Zachos, and N. J. Shackleton (2004), Astronomical calibration of the late Oligocene through early Miocene geomagnetic polarity time scale, *Earth Planet. Sci. Lett.*, *224*(12), 33–44, doi:10.1016/j.epsl.2004.05.004.

Blum, P. (1997), Physical properties handbook: A guide to the shipboard measurement of physical properties of deep-sea cores, *Tech. Note 26*, Ocean Drill. Program, College Station, Tex. (Available at http://www-odp.tamu.edu/publications/tnotes/tn26/INDEX.HTM).

Brinkhuis, H., et al. (2006), Episodic fresh surface waters in the Eocene Arctic Ocean, *Nature*, *441*, 606–609, doi:10.1038/nature04692.

DeConto, R. M., D. Pollard, and D. Harwood (2007), Sea ice feedback and Cenozoic evolution of Antarctic climate and ice sheets, *Paleoceanography*, *22*, PA3214, doi:10.1029/2006PA001350.

Dinarès-Turell, J., J. I. Baceta, V. Pujalte, X. Orue-Etxebarria, G. Bernaola, and S. Lorito (2003), Untangling the Palaeocene climatic rhythm: An astronomically calibrated early Palaeocene magnetostratigraphy and biostratigraphy at Zumaia (Basque basin, northern Spain), *Earth Planet. Sci. Lett.*, *216*(4), 483–500, doi:10.1016/S0012-821X(03)00557-0.

Frank, M., J. Backman, M. Jakobsson, K. Moran, M. O'Regan, J. King, B. A. Haley, P. W. Kubik, and D. Garbe-Schönberg (2008), Beryllium isotopes in central Arctic Ocean sediments over the past 12.3 million years: Stratigraphic and paleoclimatic implications, *Paleoceanography*, *23*, PA1S02, doi:10.1029/2007PA001478.

Gallimore, R. G., and J. E. Kutzbach (1995), Snow cover and sea ice sensitivity to generic changes in Earth orbital parameters, *J. Geophys. Res.*, *100*(D1), 1103–1120.

Ghil, M., et al. (2002), Advanced spectral methods for climatic time series, *Rev. Geophys.*, *40*(1), 1003, doi:10.1029/2000RG000092.

Hilgen, F. J. (1991), Astronomical calibration of Gauss to Matuyama sapropels in the Mediterranean and implication for the geomagnetic polarity time scale, *Earth Planet. Sci. Lett.*, *104*(2–4), 226–244, doi:10.1016/0012-821X(91)90206-W.

Huybers, P. (2006), Early Pleistocene glacial cycles and the integrated summer insolation forcing, *Science*, *313*, 508–511, doi:10.1126/science.1125249.

Huybers, P., and C. Wunsch (2005), Obliquity pacing of the late Pleistocene glacial terminations, *Nature*, *434*, 491–494, doi:10.1038/nature03401.

Jackson, C. S., and A. J. Broccoli (2003), Orbital forcing of Arctic climate: Mechanisms of climate response and implications for continental glaciation, *Clim. Dyn.*, *21*, 539–557, doi:10.1007/s00382-003-0351-3.

Jiang, N., J. D. Neelin, and M. Ghil (1995), Quasi-quadrennial and quasi-biennial variability in the equatorial Pacific, *Clim. Dyn.*, *12*, 101–112.

Krylov, A. A., I. A. Andreeva, C. Vogt, J. Backman, V. V. Krupskaya, G. E. Grikurov, K. Moran, and H. Shoji (2008), A shift in heavy and clay mineral provenance indicates a middle Miocene onset of a perennial sea ice cover in the Arctic Ocean, *Paleoceanography*, doi:10.1029/2007PA001497, in press.

Kuiper, K. F., F. J. Hilgen, J. Steenbrink, and J. R. Wijbrans (2004), $^{40}Ar/^{39}Ar$ ages of tephras intercalated in astronomically tuned Neogene sedimentary sequences in the eastern Mediterranean, *Earth Planet. Sci. Lett.*, *222*(2), 583–597, doi:10.1016/j.epsl.2004.03.005.

Laskar, J. (1999), The limits of Earth orbital calculations for geological time-scale use, *Philos. Trans. R. Soc. London, Ser. A*, *357*(1757), 1735–1759, doi:10.1098/rsta.1999.0399.

Laskar, J., F. Joutel, and F. Boudin (1993), Orbital, precessional, and insolation quantities for the Earth from −20 Myr to +10 Myr, *Astron. Astrophys.*, *270*, 522–533.

Laskar, J., P. Robutel, F. Joutel, M. Gastineau, A. Correia, and B. Levrard (2004), A long term numerical solution for the insolation quantities of the Earth, *Astron. Astrophys.*, *428*, 261–285, doi:10.1051/0004-6361:20041335.

Lourens, L. J., R. Wehausen, and H. J. Brumsack (2001), Geological constraints on tidal dissipation and dynamical ellipticity of the Earth over the past three million years, *Nature*, *409*, 1029–1033, doi:10.1038/35059062.

Lourens, L. J., F. J. Hilgen, J. Laskar, N. J. Shackleton, and D. Wilson (2005), The Neogene period, in *A Geological Time Scale 2004*, edited by F. M. Gradstein et al., pp. 409–440, Cambrige Univ. Press, New York.

Milankovitch, M. (1941), *Kanon der Erdbestrahlung und seine Anwendung auf das Eiszeitenproblem*, *Spec. Publ.*, vol. 132, R. Serb. Sci., Belgrad. (English translation Israel Program for Sci. Transl., Jerusalem, 1969).

Moran, K., et al. (2006), The Cenozoic palaeoenvironment of the Arctic Ocean, *Nature*, *441*, 601–605, doi:10.1038/nature04800.

O'Regan, M., J. W. King, J. Backman, M. Jakobsson, K. Moran, C. Heil, T. Sakamoto, T. Cronin, and R. Jordan (2008), Constraints on the Plio-Pleistocene chronology of sediments from the Lomonosov Ridge, *Paleoceanography*, doi:10.1029/2007PA001551, in press.

Pagani, M., J. C. Zachos, K. H. Freeman, B. Tipple, and S. Bohaty (2005), Marked decline in atmospheric carbon dioxide concentrations during the Paleogene, *Science*, *309*, 600–603, doi:10.1126/science.1110063.

Pälike, H., and N. J. Shackleton (2000), Constraints on astronomical parameters from the geological record for the last 25 Myr, *Earth Planet. Sci. Lett.*, *182*(1), 1–14, doi:10.1016/S0012-821X(00)00229-6.

Pälike, H., N. J. Shackleton, and U. Röhl (2001), Astronomical forcing in late Eocene marine sediments, *Earth Planet. Sci. Lett.*, *193*(34), 589–602, doi:10.1016/S0012-821X(01)00501-5.

Pälike, H., J. Laskar, and N. J. Shackleton (2004), Geologic constraints on the chaotic diffusion of the solar system, *Geology*, *32*(11), 929–932, doi:10.1130/G20750.1.

Pälike, H., R. D. Norris, J. O. Herrle, P. A. Wilson, H. K. Coxall, C. H. Lear, N. J. Shackleton, A. K. Tripati, and B. S. Wade (2006a), The heartbeat of the Oligocene climate system, *Science*, *314*, 1894–1898, doi:10.1126/science.1133822.

Pälike, H., J. Frazier, and J. C. Zachos (2006b), Extended orbitally forced palaeoclimatic records from the equatorial Atlantic Ceara Rise, *Quat. Sci. Rev.*, *25*(23–24), 3138–3149, doi:10.1016/j.quascirev.2006.02.011.

Plaut, G., and R. Vautard (1994), Spells of low-frequency oscillations and weather regimes in the Northern Hemisphere, *J. Atmos. Sci.*, *51*(2), 210–236, doi:10.1175/1520-0469(1994)051<0210:SOLFOA>2.0.CO;2.

Press, W. H., S. A. Teukolsky, W. T. Vetterling, and B. P. Flannery (1992), *Numerical Recipes in C: The Art of Scientific Computing*, 2nd ed., pp. 656–706, Cambridge Univ. Press, Cambridge, U. K.

Raffi, I., J. Backman, and H. Pälike (2005), Changes in calcareous nannofossil assemblages across the Paleocene/Eocene transition from the paleo-equatorial Pacific Ocean, *Palaeogeogr. Palaeoclimatol. Palaeoecol.*, *226*(12), 93–126, doi:10.1016/j.palaeo.2005.05.006.

Raffi, I., J. Backman, E. Fornaciari, H. Pälike, D. Rio, L. Lourens, and F. Hilgen (2006), A review of calcareous nannofossil astrobiochronology encompassing the past 25 million years, *Quat. Sci. Rev.*, *25*, 3113–3137, doi:10.1016/j.quascirev.2006.07.007.

Sangiorgi, F., H.-J. Brumsack, D. A. Willard, S. Schouten, C. E. Stickley, M. O'Regan, G.-J. Reichart, J. S. Sinninghe Damsté, and H. Brinkhuis (2008a), A 26 million year gap in the central Arctic record at the greenhouse-icehouse transition: Looking for clues, *Paleoceanography*, *23*, PA1S04, doi:10.1029/2007PA001477.

Sangiorgi, F., E. E. van Soelen, D. J. A. Spofforth, H. Plike, C. E. Stickley, K. St. John, N. Ko, S. Schouten, J. S. Sinninghe Damst, and H. Brinkhuis (2008b), Cyclicity in the middle Eocene central Arctic Ocean sediment record: Orbital forcing and environmental response, *Paleoceanography*, doi:10.1029/2007PA001487, in press.

Shackleton, N. J. (2000), The 100,000–year ice-age cycle identified and found to lag temperature, carbon dioxide, and orbital eccentricity, *Science*, *289*, 1897–1902, doi:10.1126/science.289.5486.1897.

Spofforth, D. J. A., H. Pälike, and D. Green (2008), Paleogene record of elemental concentrations in sediments from the Arctic Ocean obtained by XRF analyses, *Paleoceanography*, doi:10.1029/2007PA001489, in press.

Stein, R., B. Boucsein, and H. Meyer (2006), Anoxia and high primary production in the Paleogene central Arctic Ocean: First detailed records from Lomonosov Ridge, *Geophys. Res. Lett.*, *33*, L18606, doi:10.1029/2006GL026776.

Tiedemann, R., M. Sarnthein, and N. J. Shackleton (1994), Astronomic timescale for the Pliocene Atlantic δ^{18}O and dust flux records of Ocean Drilling Program Site 659, *Paleoceanography*, *9*(4), 619–638.

Torrence, C., and G. P. Compo (1998), A practical guide to wavelet analysis, *Bull. Am. Meteorol. Soc.*, *79*(1), 61–78, doi:10.1175/1520-0477(1998)079<0061:APGTWA>2.0.CO;2.

Tuenter, E., S. K. Weber, F. J. Hilgen, and L. J. Lourens (2005), Sea-ice feedbacks on the climatic response to precession and obliquity forcing, *Geophys. Res. Lett.*, *32*, L24704, doi:10.1029/2005GL024122.

Tukey, J. (1977), *Exploratory Data Analysis*, Addison-Wesley, Reading, Mass.

Vautard, R., and M. Ghil (1989), Singular spectrum analysis in nonlinear dynamics, with applications to paleoclimatic time series, *Physica D*, *35*, 395–424, doi:10.1016/0167-2789(89)90077-8.

Vautard, R., P. Yiou, and M. Ghil (1992), Singular-spectrum analysis: A toolkit for short, noisy chaotic signals, *Physica D*, *58*, 95–126, doi:10.1016/0167-2789(92)90103-T.

Wade, B. S., and H. Pälike (2004), Oligocene climate dynamics, *Paleoceanography*, *19*, PA4019, doi:10.1029/2004PA001042.

Weedon, G. P. (2003), *Time-Series Analysis and Cyclostratigraphy*, Cambridge Univ. Press, New York.

Wehausen, R., and H. J. Brumsack (1999), Cyclic variations in the chemical composition of eastern Mediterranean Pliocene sediments: A key for understanding sapropel formation, *Mar. Geol.*, *153*(1–4), 161–176, doi:10.1016/S0025-3227(98)00083-8.

J. Gattacceca, Geophysics and Planetology, CEREGE, CNRS, University of Aix-Marseille 3, F-13628 Aix-en-Provence, France.

M. O'Regan, Graduate School of Oceanography, University of Rhode Island, Narragansett, RI 02882, USA.

H. Pälike and D. J. A. Spofforth, National Oceanography Centre, University of Southampton, European Way, Southampton SO14 3ZH, UK. (heiko.palike@noc.soton.ac.uk)